

A finite element multifrontal method for 3D CSEM modeling in the frequency domain

Nuno Vieira da Silva¹, Joanna V. Morgan¹, Lucy MacGregor², and Mike Warner¹

ABSTRACT

There has been a recent increase in the use of controlled-source electromagnetic (CSEM) surveys in the exploration for oil and gas. We developed a modeling scheme for 3D CSEM modeling in the frequency domain. The electric field was decomposed in primary and secondary components to eliminate the singularity originated by the source term. The primary field was calculated using a closed form solution, and the secondary field was computed discretizing a second-order partial differential equation for the electric field with the edge finite element. The solution to the linear system of equations was obtained using a massive parallel multifrontal solver, because such solvers are robust for indefinite and ill-conditioned linear systems. Recent trends in parallel computing were investigated for their

use in mitigating the computational overburden associated with the use of a direct solver, and of its feasibility for 3D CSEM forward modeling with the edge finite element. The computation of the primary field was parallelized, over the computational domain and the number of sources, using a hybrid model of parallelism. When using a direct solver, the attainment of multisource solutions was only competitive if the same factors are used to achieve a solution for multi right-hand sides. This aspect was also investigated using the presented methodology. We tested our proposed approach using 1D and 3D synthetic models, and they demonstrated that it is robust and suitable for 3D CSEM modeling using a distributed memory system. The codes could thus be used to help design new surveys, as well to estimate subsurface conductivities through the implementation of an appropriate inversion scheme.

INTRODUCTION

Initially developed for defense purposes (Constable and Srnka, 2007), marine electromagnetic methods have gained attention from the oil and gas exploration industry (Ellingsrud et al., 2002; Constable, 2005; Srnka et al., 2006), particularly during the past decade. Although 3D seismic reflection data provide high resolution structural images, as well as indicators of whether geological formations contain hydrocarbons, the changes in physical properties and associated seismic response are relatively small. In addition, interpretations of amplitude variation with offset (AVO) response can be ambiguous, as other changes in rock properties can produce the same AVO characteristics (Yilmaz, 2001).

The electrical resistivity of a geological formation is essentially determined by its pore content; they exhibit a resistive anomaly when those pores are filled with oil or gas. This fact makes con-

trolled-source electromagnetic (CSEM) methods an important tool to reduce ambiguities and reduce exploratory risk.

The CSEM experiment consists of towing an electric-dipole antenna to generate an electric field, and the response of the geological formations to the excitation is recorded by electric and magnetic field receivers at the sea floor. Depending on the depth of the target, the transmitter operating frequencies may range between 0.1 and 10 Hz and the source-receiver offsets can be up to 10 km (Eidesmo et al., 2002).

The subsurface lateral variations of conductivity can be strong, especially when bathymetry is rough. Therefore, the use of full 3D CSEM forward modeling for survey design and correct data interpretation is desirable. CSEM forward modeling requires solving Maxwell's equations in the time or frequency domain. The latter is generally preferred as CSEM data is usually interpreted in terms of amplitude and phase, which are obtained using a fast Fourier

Manuscript received by the Editor 2 December 2010; revised manuscript received 2 September 2011; published online 17 February 2012.

¹Imperial College London, Department of Earth Science and Engineering, London, U. K. E-mail: n.vieira-da-silva08@imperial.ac.uk; j.v.morgan@imperial.ac.uk; m.warner@imperial.ac.uk.

²Rock Solid Images PLC, Aberdeen, U. K. E-mail: lucy.macgregor@rocksolidimages.com.

© 2012 Society of Exploration Geophysicists. All rights reserved.

transform (FFT), and inversion is generally carried out for a small number of frequencies (MacGregor et al., 2001). Forward modeling requires solving Maxwell's equations for complex-shaped structures, because geological structures generally have complicated geometries. Dyadic Green's functions (Avdeev et al., 2002; Hursan and Zhdanov, 2002) are commonly used in forward modeling due to their high computational efficiency, but the representation of models with complex geometry may be cumbersome. Some alternative methods allow complex models of resistivity with significantly less effort. Arbitrarily eliminating the magnetic field from Maxwell's equations leads to a second-order partial differential equation for the electric field, which can be discretized using the finite-difference method (FDM) (Newman and Alumbaugh, 1995) or the finite integration technique (FIT) (Plessix et al., 2007). Both methods use staggered grids as proposed by Yee (1966). Other approaches include the decomposition of the electric field in vector and scalar potentials, imposing a gauge condition and enforcing the conservation of current density (Tyler et al., 2004). Splitting the electric field into components in the active and null spaces of the discrete Maxwell's operator and using gauge conditions, leads to a more stable and strong elliptic system when compared to using a formulation with components in both spaces (Aruliah et al., 2001). The equivalent linear system can be discretized with resort to the finite volume method (FVM) (Haber et al., 2000) or using the finite element method with nodal basis functions (Badea et al., 2001).

Finite element methods, FIT, FVM, and FDM require the solution of a sparse linear system of equations. The solution of large-scale linear systems is a key aspect of numerical linear algebra because it has a major impact in the applicability and robustness of numerical solutions of partial differential equations. Krylov subspace (van der Vorst, 2003) techniques are usually preferred because the memory storage requirements are relatively modest. In the case of low-frequency electromagnetic problems, the use of Krylov subspace methods requires special preconditioning to deflate the large kernel of the curl operator (Newman and Alumbaugh, 2002). On the other hand, direct solvers are more demanding computationally and their application to 3D problems has traditionally been avoided. Recent advances in numerical factorization algorithms, along with the availability of parallel computational resources, have created the necessary conditions to attract some interest in factorization methods in the context of geophysical 3D problems. For example, Ben-Hadj-Ali et al. (2008) used a direct solver for 3D acoustic full-waveform inversion, Oldenburg et al. (2008) and Börner et al. (2008) utilized direct solvers for transient electromagnetic modeling, and Streich (2009) utilized a direct solver for CSEM modeling in the frequency domain, discretizing Maxwell's equations with the finite-difference method over a staggered grid. It is important to note that all these authors stressed the fact that direct solvers are very demanding in terms of memory requirements, thus imposing model size limitations when applied to 3D problems. Even though the stability of an algorithm does not guarantee the achievement of an accurate solution for an ill-conditioned problem, factorization methods are generally more robust to ill-conditioning (in comparison to iterative solvers), provided that sufficient arithmetic precision is used (Datta, 2010). In addition, factorization methods are well suited for multiright side problems, i.e., problems where the solution for different right sides are required but the matrix of coefficients is constant. In such problems only one factorization is necessary, and multiple solutions can be obtained by

backward and forward substitutions with minimal additional computational cost (Operto et al., 2007; Abubakar et al., 2008). Consequently, for survey simulation and data inversion where the solution for multiple sources is generally required, the use of factorization methods naturally provides a multisource solution.

There are some particular difficulties associated with the implementation of numerical schemes for 3D CSEM modeling when using the finite element method. First, the direct representation of the source vector, in terms of current density that originates from an electric dipole on the grid can produce numerical instabilities, and may require a very fine grid spacing near the source point. Second, the normal component of the electric field is discontinuous at the interfaces of mediums with different electromagnetic properties, whereas the tangential component is continuous, therefore requiring conforming discretization methods. When the air is represented in the resistivity model, two additional difficulties arise: the electric field amplitude does not decay exponentially in the air-region, and the linear system of equations is indefinite and ill-conditioned, thus having a strong impact in the accuracy of the numerical solution and performance of the solver. Finally, practical applications of CSEM modeling require the solution for several sources, thus each source solution must be obtained in an acceptable run time.

All these issues were addressed in our proposed modeling scheme. The representation of the source on the grid is addressed through decomposing the electric field into primary and secondary components (Newman and Alumbaugh, 1995). The primary field is calculated utilizing a homogeneous or horizontally layered resistivity model, for which a closed form of solution is known (Chave and Cox, 1982; Ward and Hohmann, 1988; Andreis and MacGregor, 2008). When models require the representation of air, the accuracy of solution improves significantly by including its representation in the background model, and in this case we chose to use a background model with two half-spaces. The interface between half-spaces is coincident with the air-sea interface. This requires the computation of Hankel transforms (Anderson, 1979), which is very intensive computationally, and therefore the acceleration of its computation using a shared memory model of parallelism is investigated. For the numerical discretization of the Maxwell equation for the electric field, we considered Nedelec's finite element (Nedelec, 1980) which satisfies the electric field interface conditions and implicitly enforces locally the divergence-free condition. In addition, and in comparison to existing schemes such as the finite-difference method with staggered grids, the edge finite element does not require averaging schemes for the material properties (Alumbaugh et al., 1996), and therefore, has the advantage of only requiring a single value for the resistivity of each cell. Finally, to solve the linear system we utilized a massive parallel implementation of a multifrontal solver: MUMPS (Amestoy et al., 2000, 2001). MUMPS remains robust when the air is included in the model, and when the grid has large aspect ratios. During our study, tests showed that the latter was the main cause of slow convergence, when iterative solvers were used with the edge finite element scheme. As direct solvers are known to be computationally intensive, a hybrid model of parallelism was used to minimize the memory and message passing overhead and, a scalability study has been performed to investigate its efficiency. In the last section of this manuscript, an example is presented, showing the application of the presented modeling approach for the solution of a multisource problem. The computation of the primary field is parallelized over the

number of edges for one source, using a shared memory model of parallelism, and is parallelized over the number of sources using a distributed memory model of parallelism. The linear system is factorized using MUMPS and the factors are reutilized for the computation of the solution for multiple right hand sides. The paper starts with a summary of the relevant electromagnetic theory. This is followed by a description of the numerical discretization of the partial differential equation for the secondary electric field in the diffusive regime, using Nedelec's elements, and analysis of the numerical solution of the linear system presenting a scalability study. We then run a suite of forward modeling tests to validate our numerical scheme, using a 1D model with a thin resistive layer and 3D model with a thin resistive block. Finally an example is presented for the case of multiple sources.

BACKGROUND THEORY AND APPROACH

The equations of Maxwell for an isotropic conductive medium, with harmonic temporal dependency $e^{-i\omega t}$ (Jackson, 1998) read:

$$\nabla \times \mathbf{E} = i\omega\mu\mathbf{H}, \quad (1a)$$

$$\nabla \times \mathbf{H} - (\sigma - i\omega\epsilon)\mathbf{E} = \mathbf{J}. \quad (1b)$$

The mathematical symbols are listed in Table 1. The magnetic permeability μ is considered constant and equal to the magnetic permeability in a vacuum. Discretizing the system of equations 1 with the finite element method has the inconvenience of requiring a consistent discretization for magnetic and electric fields (Rodrigue and White, 2001). Furthermore, solving the coupled system of equations for the fields in the air leads to a weak coupling, because the conduction term from Faraday's law vanishes. This problem can be addressed by arbitrarily eliminating one of the fields in system 1 (Newman and Alumbaugh, 1995), leading to a second-order partial differential equation for the electric field:

$$\nabla \times \nabla \times \mathbf{E} - \omega\mu(\omega\epsilon + i\sigma)\mathbf{E} = i\omega\mu\mathbf{J}_s. \quad (2)$$

Using equation 2 also has the advantage of reducing the number of degrees of freedom in the linear system derived from the numerical discretization, in comparison to the use of the first-order linear system or the use of potentials (Um et al., 2010), and therefore requiring less storage. For a complete formulation and to ensure the uniqueness of the solution, the perfect electrically conductive boundary condition is considered:

$$\mathbf{n} \times \mathbf{E} |_{\partial\Omega} = \mathbf{0}. \quad (3)$$

The truncation of the computational domain with boundary condition 3 does not cause reflections in the solution because the electric field amplitude decays exponentially in the diffusive regime (Druskin et al., 1999), thus it can be imposed in a region away from heterogeneities (Spichak, 2006). Even though the electric field amplitude does not decay exponentially in the air region, from our experience the boundary can be truncated, provided that the grid is severely stretched near the boundary and that the air layer is represented in the background model.

The current density term, \mathbf{J}_s , is generally represented by a point source or a line of point sources in the frequency domain, and its direct numerical representation on a grid can lead to additional

difficulties, namely numerical instabilities and phase inaccuracy. The decomposition of the primary field into primary and secondary components alleviates these difficulties (Newman and Alumbaugh, 1995).

Typically only low frequencies are used in the CSEM experiment and therefore displacement currents can be neglected because the inequality $\sigma/(\omega\epsilon) \gg 1$ holds. A similar analysis can be accomplished using Maxwell's equations in their original form. By plugging $\mathbf{E} = \mathbf{E}_p + \mathbf{E}_s$ and $\Delta\sigma = \sigma - \sigma_p$ into equation 2 and considering the quasi-static limit approximation it is possible to derive the equation for the secondary electric field:

$$\nabla \times \nabla \times \mathbf{E}_s - i\omega\mu\sigma\mathbf{E}_s = i\omega\mu\Delta\sigma\mathbf{E}_p. \quad (4)$$

Generally, in CSEM surveys the source fields are generated by finite length dipoles, thus the point source approximation may not be the most exact representation of a real source. However, as pointed out by Streich and Becken (2011), the fields generated by a point source and by a 300 m length wire are nearly identical at radii larger than 1 km, thus they are nearly identical in the range of offsets typically

Table 1. Mathematical symbols.

\mathbf{E}	Electric field
\mathbf{E}_p	Primary electric field
\mathbf{E}_s	Secondary electric field
\mathbf{J}_s	Current density
\mathbf{H}	Magnetic field
σ	Conductivity distribution
ρ	Resistivity distribution
σ_p	Background model conductivity
$\Delta\sigma = \sigma - \sigma_p$	Conductivity anomaly
μ	Magnetic permeability
ϵ	Electric permittivity
ω	Angular frequency
i	Imaginary unit
$\partial\Omega$	Boundary of the computational domain
\mathbf{n}	Normal vector to a surface
N_e	Total number of elements
Ω^e	Polyhedral domain of a finite element
Ω	Computational domain
\mathcal{R}_k	Weighted residual
K^e	Discrete form for the curl-curl operator
M^e	Mass matrix
\mathbf{N}_i	Basis function for the i th edge
(ξ, η, ζ)	Local coordinate system of an element
(ξ_i, η_i, ζ_i)	Local coordinates of the center for the i th edge on an element
l_x^e, l_y^e, l_z^e	Lengths of an element in the x -, y -, and z -directions, respectively
$\mathbf{x} = (x^e, y^e, z^e)$	General physical coordinates for element e
$\mathbf{x}_i = (x_c^e, y_c^e, z_c^e)$	Coordinate of the center of the element e

used in hydrocarbon exploration. In addition, for a 100 m length electric dipole, typically used for gas hydrates exploration, the electromagnetic fields are also identical within the range of offsets used to detect the resistivity anomaly that is produced by the existence of gas hydrates. [Streich and Becken \(2011\)](#) also stressed the fact that moderate distortions in the source shape can be disregarded when compared with the accuracy of the source orientation. Hence, the point source approximation can be considered a good representation of the real sources utilized in marine CSEM surveys. For the reasons aforementioned, only point sources will be considered in this work. The primary field can be calculated for a simple model with conductivity distribution σ_p for which a closed form of the solution is known, such as the solution for the electric field generated by an electric dipole in a homogeneous medium ([Ward and Hohmann, 1988](#)), or in a horizontally layered medium ([Chave and Cox, 1982](#); [Andreis and MacGregor, 2008](#)). The secondary electric field is calculated by numerically solving equation 4, using the finite element method. After the calculation of the electric field, the magnetic field can be calculated from Faraday's law:

$$\mathbf{H} = (i\mu\omega)^{-1} \nabla \times \mathbf{E}. \quad (5)$$

Considering the finite element framework one could derive an equivalent weak form for equation 5. Nonetheless, adopting such an approach requires solving a linear system of equations, and from our experience that may produce numerical oscillations near the source position and inaccuracies near the boundary. Therefore, we decided to use a local finite-difference approximation of Faraday's law using the values of the electric field discretized at the edges and interpolate it to the receiver point ([Alumbaugh et al., 1996](#)). The electric and the magnetic fields are interpolated at the receiver point using trilinear interpolation.

NUMERICAL DISCRETIZATION

The discretization of equation 4 with nodal finite elements is known to lead to nonphysical solutions, also known as spurious modes, because such an approach does not enforce the divergence-free condition and does not allow for the discontinuity of the normal component of the electric field at interfaces between different materials ([Jin, 2002](#); [Bondeson et al., 2005](#)). The existence of spurious modes in the solution can be avoided by the use of Nedelec's elements (or edge elements), which consist of assigning the degrees of freedom to edges instead of the nodes ([Nedelec, 1980](#); [Monk, 2003](#)). For the implementation of our scheme, we

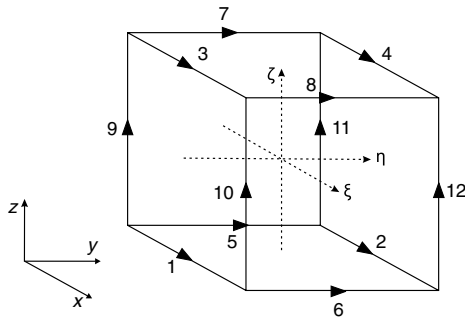


Figure 1. Illustration of an arbitrary hexahedron with a local frame of reference (ξ, η, ζ) , and numbering of the electric field sampling positions at the center of the edges.

considered structured grids because they can easily be implemented using a Cartesian product of the coordinates in each orthogonal direction in space ([Liseikin, 2009](#)), thus our computational domain is decomposed using hexahedra. The use of Cartesian conforming hexahedra has the main advantage of allowing the generation of grids without significant effort. The maximum grid spacing can be determined from the skin depth for a certain resistivity model and frequency $\delta \approx 500 \sqrt{\rho/f}$ ([Plessix et al., 2007](#)). Complex structures can be approximated through stair-casing multiple elements of constant resistivity or by using varying conductivity inside the finite elements. However, the last feature was not implemented here. In addition, and as aforementioned, the presented scheme does not require averaging schemes for the material properties as in the case of the finite-difference method on a staggered grid ([Alumbaugh et al., 1996](#)).

Each arbitrary hexahedron in space can be mapped to a reference eight node hexahedron for which we define a local frame with coordinates (ξ, η, ζ) such that $\xi, \eta, \zeta \in [-1, 1]$, through the mapping:

$$\begin{aligned} \xi &= \frac{2(x^e - x_c^e)}{l_x^e}, \\ \eta &= \frac{2(y^e - y_c^e)}{l_y^e}, \\ \zeta &= \frac{2(z^e - z_c^e)}{l_z^e}. \end{aligned} \quad (6)$$

Figure 1 shows an arbitrary hexahedron with its local frame of reference, (ξ, η, ζ) . A first-order basis for a reference hexahedron is given by

$$\mathbf{N}_i = \frac{l_i^e}{8} (1 + \eta_i \eta) (1 + \zeta_i \zeta) \nabla \xi, \quad (7)$$

where $i \in \{1, \dots, 4\}$, correspond to the ξ oriented edges,

$$\mathbf{N}_i = \frac{l_i^e}{8} (1 + \xi_i \xi) (1 + \zeta_i \zeta) \nabla \eta, \quad (8)$$

where $i \in \{5, \dots, 8\}$, correspond to the η oriented edges, and

$$\mathbf{N}_i = \frac{l_i^e}{8} (1 + \xi_i \xi) (1 + \eta_i \eta) \nabla \zeta, \quad (9)$$

where $i \in \{9, \dots, 12\}$, for the ζ oriented edges. The superscript e is the element ordering. Using edge finite elements and Galerkin's method ([Zienkiewicz and Taylor, 2005](#)), the weak form equivalent to equation 4 holds:

$$\mathcal{R}_k = \int_{\Omega} \mathbf{N}_k \cdot [\nabla \times \nabla \times \mathbf{E}_s - i\omega\mu\sigma\mathbf{E}_s - i\omega\mu\Delta\sigma\mathbf{E}_p] dV. \quad (10)$$

Because $\Omega = \cup_{e=1}^{N_e} \Omega^e$ equation 10 can be written in the equivalent discrete form:

$$\mathcal{R}_k = \sum_{e=1}^{N_e} [K^e E^e - i\omega\mu\sigma M^e E^e - i\omega\mu\Delta\sigma M^e E_p^e]. \quad (11)$$

Equation 11 is also known as the assembly of elemental matrices in the global system of equations. The element submatrices K^e and M^e are given by:

$$K_{kl}^e = \int_{\Omega^e} (\nabla \times \mathbf{N}_k) \cdot (\nabla \times \mathbf{N}_l) dV, \quad (12)$$

$$M_{kl}^e = \int_{\Omega^e} \mathbf{N}_k \cdot \mathbf{N}_l dV. \quad (13)$$

For the calculation of the integrals in equations 12 and 13, we derived analytical expressions using a computer algebra system instead of using numerical integration, because we are not considering adaptive grids. We refer to the work by Jin (2002) for further details on the construction of the basis functions, as well integration and assembly of the linear system of equations.

The edges are numbered by sequentially assigning a number to each of the x , y , and z oriented edges (and by this order) which share the same node, and repeating for all nodes. The sparsity pattern for this ordering is shown in Figure 2 for a small grid ($9 \times 9 \times 11$), and the bandwidth is approximately $6N_x N_y$, where N_x and N_y are the number of nodes in the x - and y -directions of a structured grid.

SOLUTION OF THE LINEAR SYSTEM OF EQUATIONS

The discretization of the secondary electric field equation leads to a large, sparse, complex-valued, symmetric, ill-conditioned, and linear system of equations

$$\mathbf{A}\mathbf{e} = \mathbf{s} \quad (14)$$

where \mathbf{A} is the matrix resulting from the discretization of equation 4 with edge finite elements and is also known as the stiffness matrix, \mathbf{e} is the unknown secondary electric field at the center of the edges, and \mathbf{s} is the source vector resulting from the term on the right side of equation 4.

Iterative solvers such as Krylov subspace methods (van der Vorst, 2003) are an attractive approach for solving linear systems because their implementation relies essentially on matrix to vector multiplications and therefore are undemanding in terms of storage requirements and computational complexity. However, without effective preconditioning, the number of iterations necessary to achieve convergence can be considerably high, or convergence may not be achieved, particularly for linear systems such as equation 14 that can be indefinite for very low frequency or when $\sigma = 0$ (Saad, 2003). To accelerate the convergence to a solution, iterative solvers require effective preconditioning. For example, Torquil Smith (1996) introduced the static divergence correction, which corrects the approximate solution of the electric field to a divergence-free electric field solution, at each iteration, and Newman and Alumbaugh (2002) introduced the low induction number (LIN) preconditioner which deflates the large null-space associated to the curl operator. In Torquil Smith (1996) and Newman and Alumbaugh (2002), Maxwell's equations are discretized with the finite-difference method. During this study, it was noticed that the main factor associated to slow convergence rates, when using an iterative solver for the solution of equation 14, is the presence of large aspect ratios in the grid, due to the refinement of the grid in the vicinity of the source position.

In recent years, a substantial improvement has been made regarding the development of efficient and scalable sparse matrix factorization algorithms. Furthermore, there has been a considerable

improvement in the available hardware, namely increasing processing speeds, available memory, and hard disk reading technology, making the efficient implementation of out-of-core technology possible.

Sparse direct solvers commonly involve four main tasks: an ordering stage that exploits the sparsity pattern of the matrix followed by an analysis phase, or symbolic factorization step, which determines a pivot sequence and internal data structures. The first two steps are crucial for memory use optimization (as an optimal ordering can reduce significantly the number of fill-ins in the matrix factors) (Germouche et al., 2003), to reduce the number of operations and to avoid null pivots which could jeopardize the stability of the solver. We obtained the best computational performance in terms of computational time and memory requirements using an implementation of multilevel partitioning methods (Karypis and Kumar, 1998). The third step consists of factorizing the matrix by using one of the many available methods, such as supernodal right or left looking or multifrontal. The factorization methods only differ in the order by which the matrix entries are accessed and updated. Direct solvers have been traditionally avoided due to their computational complexity and hardware requirements. Direct solvers, however, are robust for linear systems with high condition numbers, and for the solution of linear systems with several right-hand sides, only one factorization is required. In the case of indefinite linear systems, special care must be taken before the factorization of the frontal matrices, as the pivot sequence determined during the analysis stage may contain null pivots or pivots with a small magnitude. The existence of such pivots may jeopardize the stability of the solution and therefore require the use of special techniques. A possible remedy is the use of stable 1×1 pivots in the main diagonal, i.e., a pivot is only chosen if its absolute value is higher by a certain threshold factor, than the entry with maximum absolute magnitude in the same column. To preserve symmetry, this method is generally extended to 2×2 pivoting on the dense diagonal blocks (Bunch and Kaufmann, 1977; Gould et al., 2005); this strategy is implemented in MUMPS (Chowdhury and L'Excellent, 2010).

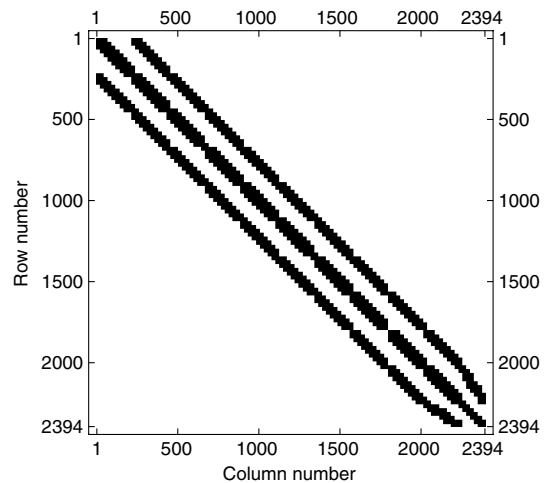


Figure 2. Sparsity pattern for the stiffness matrix obtained from the discretization with the finite element method. The size of the grid is $9 \times 9 \times 11$. The bandwidth is approximately $6N_x N_y$.

The linear system can also be symmetrically scaled to improve its numerical properties; however, we did not implement its scaling because the MUMPS numerical library allows matrix scaling. The fourth and final stage involves solving the linear system by back substituting the stored factors. Some additional and optional steps, which improve the numerical scheme, can be used such as matrix scaling prior to factorization and iterative refinement of the linear system solution during the last stage.

In the solution of all the presented examples, we used the freely available massive parallel multifrontal solver implementation MUMPS (Amestoy et al., 2000, 2001). In Appendix A, we describe a short review of the multifrontal method.

PARALLEL SOLUTION AND SCALABILITY STUDY

Real geophysical surveys are massive in spatial coverage and data volume. Therefore, in the current computational state of the art, parallel computing systems are often necessary to achieve results with acceptable running times, with distributed memory systems being the most appealing alternative. In this framework, direct solvers can be a viable option, and will impose the parallelization philosophy to be adopted, because all computational nodes need to be active during the factorization stage.

In the scope of this work, we took advantage of the hybrid model of parallelism used in MUMPS. MUMPS is coded to use shared and distributed memory paradigms (Chowdhury and L'Excellent, 2010). In addition, the calculation of the primary field for each source is assigned to a different computational node. In this work, we only consider the cases of homogeneous or two-half-space background models. Solutions for the electric field in these configurations can be found in the work of Ward and Hohmann (1988); Chave and Cox (1982) and Andreis and MacGregor (2008).

Because the primary field needs to be calculated at the center of each edge, a natural approach is to parallelize its calculation over the number of edges with openMP directives, allowing to take full advantage of modern multicore processor architectures. When a two-half-space model is used for the calculation of the primary field, this aspect is particularly important as the computation of the primary field is very intensive computationally, due to the

calculation of Hankel transforms through digital filtering (Anderson, 1979). Table 2, shows the acceleration of the calculation of the primary field for one single source, with the increasing number of threads, for two different grids with different size, for homogeneous and two-half-space background models.

A critical part of this work is that we should be able to achieve a solution to realistic sized problems in a reasonable run time, as direct solvers require a huge number of floating point operations and an enormous amount of available memory. When multifrontal methods are utilized for the solution of linear systems derived from the discretization of 3D problems, the number of floating point operations and allocated memory is in the order of $\mathcal{O}(N^6)$ and $\mathcal{O}(N^4)$, respectively (Ashcraft and Liu, 1998), where N is the number of degrees of freedom in the linear system. For all the examples presented in this work, the tasks were distributed up to a maximum of 32 computational nodes, each with two Intel Xeon® 2.66 GHz Quad-Core processors, and 8 GB of RAM per node.

For the scalability study, it is considered a frame of reference with the z -axis origin at the sea-floor level and pointing upward, and a 1D model consisting of a 10 Ωm and 200 m thick layer embedded in a 1 Ωm half-space. The top of the resistive layer is 200 m below the sea floor. The sea water is represented by a half-space with resistivity 0.33 Ωm . The source is a 1 Hz electric dipole oriented in the x -direction located at (0, 0, 30) m. Table 3 shows the run times and the amount of memory allocated on each computational node for different grid sizes and different number of MPI processes (with eight threads each). Figures 3, 4 and 5 illustrate the data in Table 3. All the calculations were performed in double complex arithmetic due to the dynamic range of the electric field amplitudes. Generally, we observe that there is a good speed-up as we increase the number of nodes, and that a limit is reached beyond which adding computing nodes has little effect (Figures 3 and 4) because the execution becomes dominated by message passing. For the examples with grid size $75 \times 75 \times 37$, $95 \times 95 \times 37$, and $135 \times 135 \times 37$, the computation time increases slightly when the number of computing nodes is larger (see Table 3) because the allocated computational resources are excessively large for the dimensions of the linear system that is being solved, leading to additional message passing overhead and consequently an increase in the run-time. Nonetheless, going beyond that limit decreases the average allocated memory per node up to a factor of two, and this may help to prevent the system running out of memory, which may happen even if the out-of-core option is utilized. Therefore, we conclude that the memory scales better with the number of computational nodes than the run time.

Another important aspect of the scalability study is to know how the size of the problem scales with the number of added computer nodes. Figures 6 and 7, show how the global workspace storage and the number of floating point operations depend on the number of degrees of freedom in the linear system. There is a polynomial relationship between these two parameters and the size N of the problem, as expected from the theoretical limits referred to above. From Figures 6 and 7, one cannot expect to solve indefinitely larger problems by just increasing the computational resources and, keeping the current state of the art of factorization algorithms, nonetheless considering the examples presented in the previous section, one may conclude that it is possible to consider a multifrontal solver even when several millions of variables are involved, provided that sufficient computational resources are available.

Table 2. Acceleration ratios for the calculation of the primary field with the number of threads.

N_{threads}	Grid: $61 \times 61 \times 31$	Grid: $121 \times 121 \times 61$
	Acceleration ratio	Acceleration ratio
Homogeneous model		
1	1	1
2	1.48	1.81
4	3.70	3.92
8	7.40	6.71
Two-half-space		
1	1	1
2	1.96	1.96
4	3.87	3.85
8	7.12	7.25

MODEL EXAMPLES

Model with a thin resistive layer

To validate the proposed numerical scheme for CSEM modeling in the frequency domain, let us consider the resistivity model in Figure 8. We considered a frame of reference with the z -axis origin at the sea-floor level and pointing upward. The source is

Table 3. Scalability study for the parallel solution. $N_x \times N_y \times N_z$: grid dimension, DOF: degrees of freedom, N_{mpi} : number of MPI processes, T_f : time for factorization, T_b : time for back-substitution, M_{node} : average allocated memory per node. (–) Not enough memory; \diamond Test disregarded.

$N_x \times N_y \times N_z$	DOF	N_{mpi}	T_f/s	T_b/s	M_{node}/GB
$75 \times 75 \times 37$	613,200	1	267	6.8	2.2
		4	131	3.6	1.91
		8	69	4	1.05
		12	68	2.9	1.04
		18	69	5.5	0.77
		24	83	6.5	0.54
$95 \times 95 \times 37$	985,720	32	\diamond	\diamond	\diamond
		1	533	12	3.35
		4	232	9	2.89
		8	168	5.7	1.95
		12	145	6.15	1.7
		18	126	7.6	1.25
$135 \times 135 \times 37$	1994760	24	152	6.9	0.82
		32	\diamond	\diamond	\diamond
		1	1599	618	7.05
		4	660	31	6.13
		8	436	16	4.33
		12	433	12	3.44
$153 \times 108 \times 69$	3385935	18	268	8.63	2.58
		24	346	12	1.8
		32	328	8.8	1.43
		1	–	–	–
		4	–	–	–
		8	2144	75	11.2
$153 \times 134 \times 69$	4203609	12	1936	59	8.73
		18	1621	27	6.61
		24	1517	24	4.71
		32	1215	20	3.33
		1	–	–	–
		4	–	–	–
		8	4248	228	15
		12	2400	108	12.2
		18	2321	51	8.95
		24	2344	37	6.26
		32	2165	26	4.44

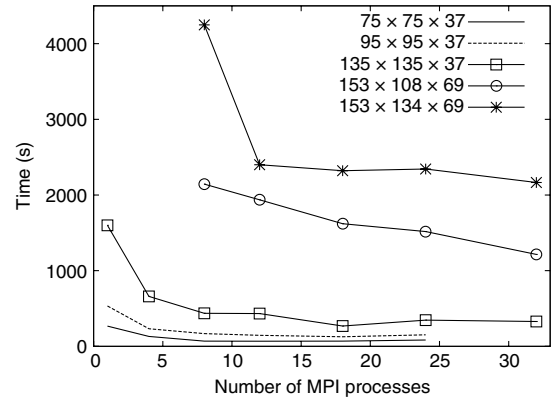


Figure 3. Comparison of the factorization times using different grid sizes, and their dependence with the number of computing nodes using a distributed memory system interconnected with GigaBit network. The corresponding data is listed in Table 3.

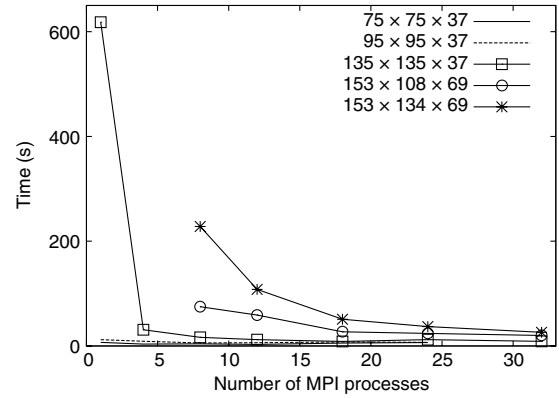


Figure 4. Comparison of the times for back-substitution using different grid sizes, and their dependence with the number of computing nodes using a distributed memory system interconnected with GigaBit network. The corresponding data is listed in Table 3.

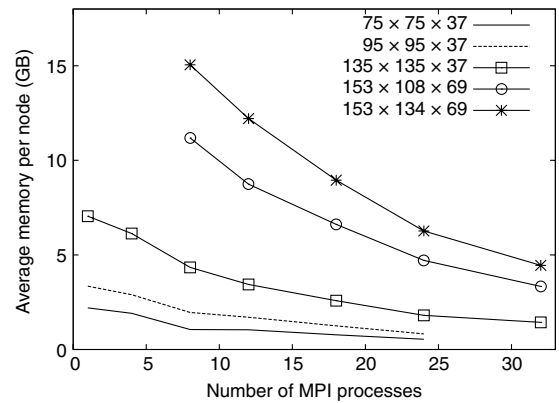


Figure 5. Comparison of the average memory allocated per computing node, and their dependence with the number of computing nodes using a distributed memory system interconnected with GigaBit network. The corresponding data is listed in Table 3.

a x -oriented electric dipole with a frequency of 0.25 Hz and located at (0,0,30) m. The model was discretized with a $141 \times 103 \times 51$ irregular mesh, representing a computational domain of $20 \times 16.4 \times 7.0$ km³ and approximately 2.2×10^6 degrees of freedom. Figure 9 shows a slice of the grid used to compute the electric and magnetic field responses using the edge finite element scheme, for the resistivity model illustrated in Figure 8. Near the source position, the grid is made finer to capture the rapid variation in the electric field in space, as the chosen finite element basis is of first order. The grid spacing ranges between 10 and 200 m. The growth ratio between adjacent elements is based on the edge length in each direction, and it is chosen not to be higher than 1.5, as this value allowed us to achieve the best results in terms of accuracy. The use of nonuniform grid spacing has the advantage of reducing the number of discretization points in the grid. The background resistivity model is homogeneous and has the same resistivity as the sea water ($0.3125 \Omega\text{m}$). The solution of the resulting linear system was distributed over 10 nodes with 8 cores each, totaling 80 processors. The factorization and back-substitution took 575 s and 12 s, respectively. Each node, on average, allocated 6.1 GB of memory.

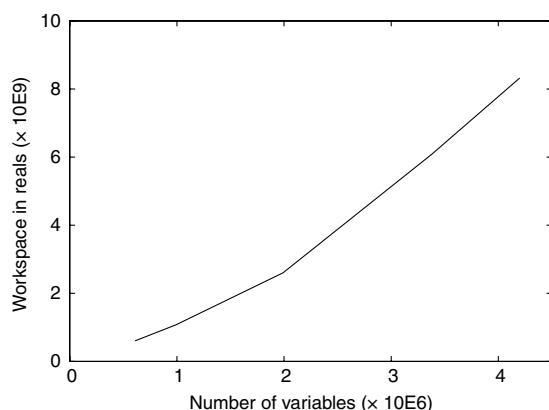


Figure 6. Dependence of the workspace storage with the number of variables in the linear system 14.

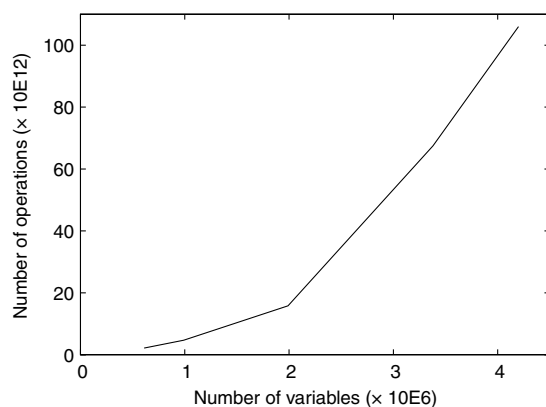


Figure 7. Dependence of the number of floating point operations with the size of the linear system 14.

The model responses obtained through the use of the proposed finite element scheme are compared with the model responses calculated using a 1D code based on [Chave and Cox's \(1982\)](#) method of solution for 1D models. Figure 10 shows the response of the electric field in terms of amplitude and phase for the model showed in Figure 8. The responses are plotted along the receiver line $y = 0$ m, for both x - and z -components. Figure 11, shows the response for the magnetic field. The responses for the magnetic field are plotted along the receiver line $y = 260$ m for the x -component, and along the receiver line $y = 500$ m for the z -component. The phase is plotted unwrapped in all the figures. The respective relative errors for amplitude and phase for electric and magnetic fields are plotted in Figure 12. The error level for the amplitude and phase of the electric and magnetic fields is below 5% in the computational region of interest, which is very good. The relatively larger errors observed in the vicinity of the source position are controlled by two main factors. First, the sea-bottom is close to the source position, thus the primary field changes rapidly in a region of anomalous resistivity, and consequently the secondary field also has a strong spatial variation in the vicinity of the source. Secondly, we used a first-order finite-element basis which has difficulty in capturing the strong spatial variation of the electric field in this region of the model. From the computational point of view, we can consider the accuracy of the solution very good for the electric and magnetic fields. In addition, the magnetic field is calculated from the numerical solution for the electric field using an interpolator and a local finite-difference for Faraday's law (equation 5).

Figure 12 shows that this approach is suitable for the calculation of the magnetic field, as the magnitude of the errors are generally below 5%, and there is a very good agreement between the approximated solution utilizing the edge finite element method and the 1D solution even in the vicinity of the source where the electric fields changes more rapidly. In the context of application to inversion of CSEM data, we still can consider a very good level of accuracy as any real data set with 5% of uncertainty would still be considered a good quality data set ([Behrens, 2005](#)). In the case of an experiment where repeatability is required, as in the case of time-lapse reservoir monitoring, measurement repeatability should be better than 5% ([Orange et al., 2009](#)). However, as [Orange et al. \(2009\)](#) stated, there are several factors which can produce discrepancies larger than 5%, as near-surface inhomogeneities, bad representation of the ocean conductivity, and inaccuracy in the position of sources and receivers. Thus, the level of accuracy obtained with the proposed methodology can be considered good in the framework of the available technology for CSEM data acquisition. For the reasons above stated, we think that there is a very good agreement between the

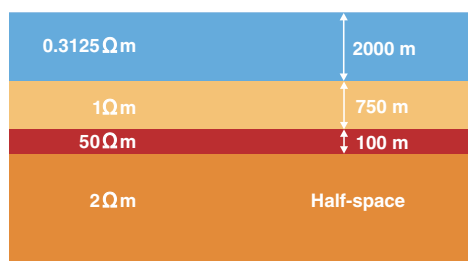


Figure 8. Illustration of the 1D model used to validate the proposed finite element scheme.

solution obtained with the edge finite element and the 1D solutions. In addition, considering the level of accuracy, the proposed methodology is suitable for applications to aid real data interpretation.

Three-dimensional model

We now show a 3D resistivity model example with the air represented. Our numerical results are compared with the ones obtained using an integral equation solution code (Hursan and Zhdanov, 2002; Zhdanov et al., 2006). As in the model in the previous section, we considered a frame of reference with the z -origin at

the sea-floor level, all z -positive values above the sea floor, and all z -negative values below the sea floor. Figure 13 shows a representation of the 3D model (truncated at the air-sea interface). The seawater column is 1000 m thick.

In our example, we used a flat sea floor to ensure that the geometry in our model could be easily compared with the solution using the integral equation method. The effective representation of bathymetry will be considered in future work. In our examples, we considered an electric-dipole source oriented in the x -direction, represented by a point source in the frequency domain, at (0,0,5) m. Here, we present two modeling examples using two frequencies —

1 Hz and 0.1 Hz — that are typical of frequencies used in the CSEM experiment.

To compute the model responses for a frequency of 1 Hz, the model was discretized using a $148 \times 150 \times 65$ irregularly spaced grid (ranging between 10 and 150 m), finer near the source position (similarly to the grid shown in Figure 9), representing a computational domain of $20 \times 20 \times 15.5 \text{ km}^3$ and approximately 4.29×10^6 degrees of freedom in double complex arithmetic. The air was represented with a 10 km thick and $10^4 \Omega\text{m}$ resistivity layer. For the calculation of the primary field, we considered a two-half-space background model, and the boundary between the half-spaces matched the air-sea interface. The upper half-space was considered resistive, and the conductivity of the lower half-space was considered equal to the seawater conductivity for this model $0.3215 \Omega\text{m}$. The solution of the resulting linear system was distributed over 24 computational nodes with eight cores each, totalizing 192 processors. The factorization took 2351 s and the back-substitution took 36 s. Each node, on average, allocated 7.1 GB of memory. The integral

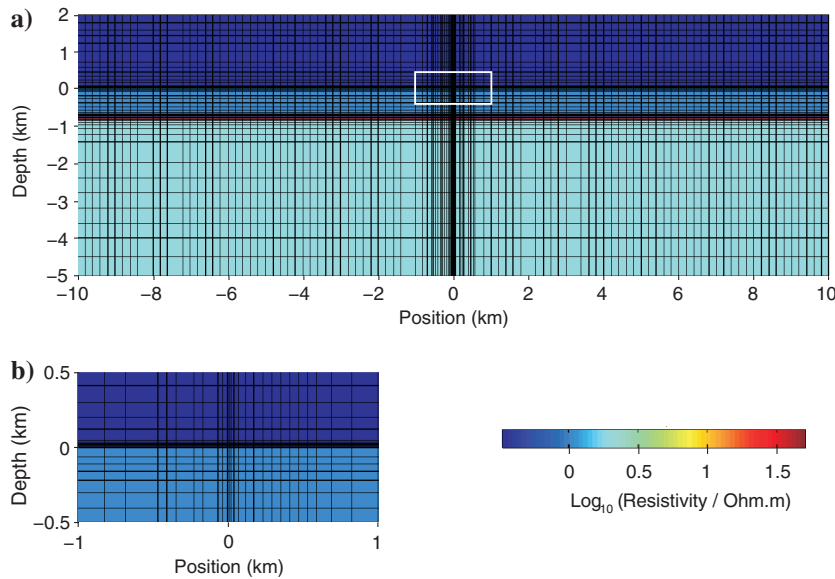


Figure 9. Slice of the grid used for the discretization of the resistivity model showed in Figure 8, (a) in the plane $y = 0 \text{ m}$, and (b) excerpt of the grid in the vicinity of the source, corresponding to the area delimited by the white rectangle in (a).

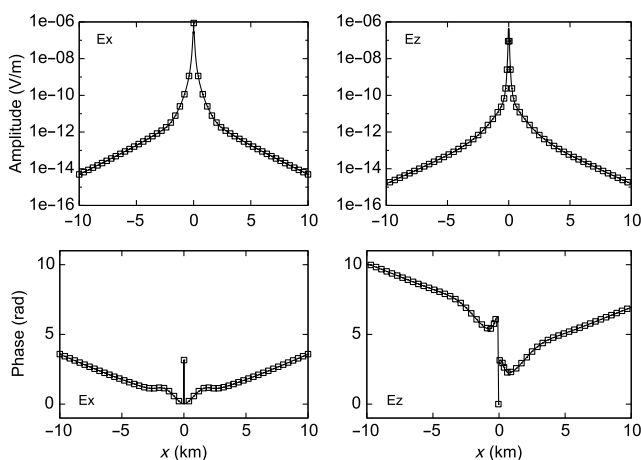


Figure 10. Comparison of the electric field responses for the model in Figure 8 calculated using the finite element method (line) and the 1D solution of Chave and Cox (1982) (open squares). The phase is unwrapped and the frequency is 0.25 Hz. The field values are plotted along the receiver line $y = 0 \text{ m}$, for both components.

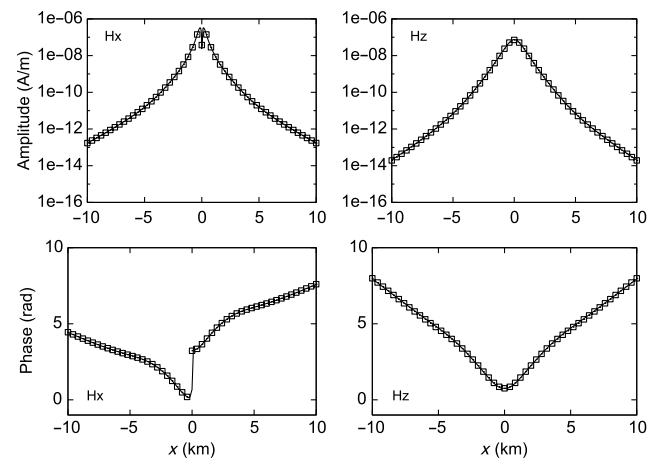


Figure 11. Comparison of the magnetic field responses for the model in Figure 8 calculated using the finite element method (line) and the 1D solution of Chave and Cox (1982) (open squares). The phase is unwrapped and the frequency is 0.25 Hz. The field values are plotted along the receiver lines $y = 260 \text{ m}$, for the x -component, and $y = 500 \text{ m}$ for the z -component.

equation code allocated approximately 330 MB of memory and took 70 s to run.

Figure 14, shows the response of the electric field in terms of amplitude and phase for a source frequency of 1 Hz. The amplitude and phase values for the x -component are plotted along the receiver line $y = 0$ m, and the y -component values are plotted along the receiver line $x = 500$ m. Figure 15, shows the response of the magnetic field for a source with 1 Hz. The amplitude and phase values for the x -component are plotted along the receiver line $y = 500$ m, and the values for the y -component are plotted along the receiver line $x = 500$ m. The phase is plotted unwrapped for all components of the electric and magnetic fields.

For a frequency of 0.1 Hz, the model was discretized with a $153 \times 108 \times 69$ irregularly spaced grid, finer near the source as in the previous examples, representing a computational domain of $23 \times 16 \times 20.6$ km³ and approximately 3.39×10^6 degrees of freedom in double complex arithmetic. The air was represented with

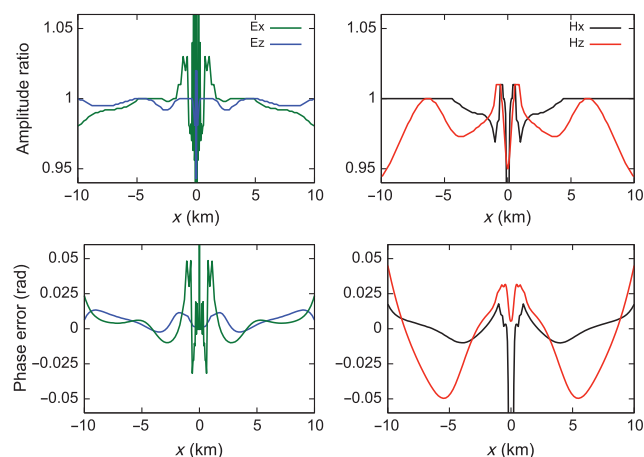


Figure 12. Plot of the relative error for the amplitude and phase of the electric and magnetic fields with respect to Figures 10 and 11.

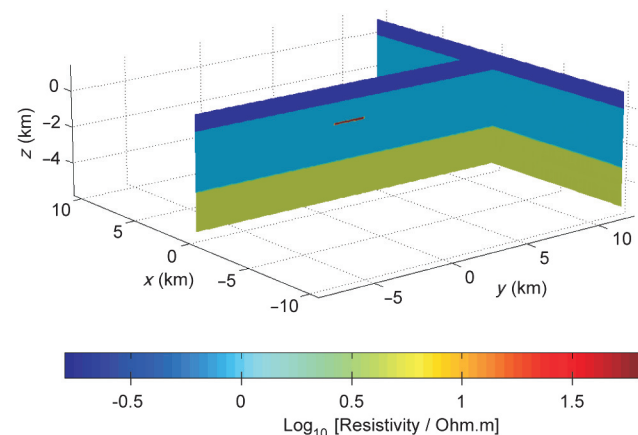


Figure 13. Three-dimensional resistivity model. The seawater is 1000 m thick. The air is not represented in the figure. The seawater resistivity is $0.3125 \Omega\text{m}$. The block with resistivity $50 \Omega\text{m}$ is embedded in a layer with resistivity $1 \Omega\text{m}$, and the resistivity of the layer at the bottom of the model is $5 \Omega\text{m}$. The color bar represents the Log_{10} of the resistivity.

a 10 km thick and $10^4 \Omega\text{m}$ resistive layer. The grid spacing ranges between 10 and 250 m. The Nyquist criterion is satisfied in the coarser regions of the grid, allowing to have less degrees of freedom compared with the grid utilized for 1 Hz. The solution of the resulting linear system was distributed over 28 nodes with eight cores each, totalizing 192 processors. The factorization and back-substitution took 1489 s and 22 s, respectively. Each node averagely allocated 4.8 GB of memory. Figure 16 shows the response of the electric field for an x -oriented electric dipole with frequency of 0.1 Hz. The amplitude and phase values for the x -component are plotted along the receiver line $y = 0$ m, and the y -component values are plotted along the receiver line $y = 500$ m. Figure 17 shows the response of the magnetic field

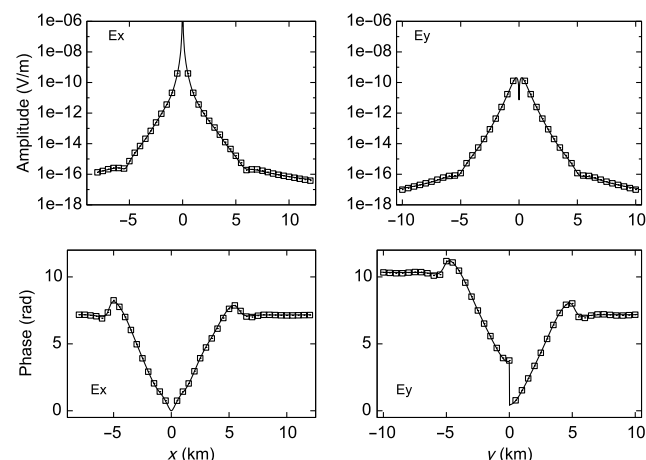


Figure 14. Comparison of the electric field responses for the model in Figure 13 calculated using the finite element method (line) and the integral equation method (open squares). The phase is unwrapped and the frequency is 1 Hz. The field values for the x -component and y -components are plotted along the receiver lines $y = 0$ m and $x = 500$ m, respectively.

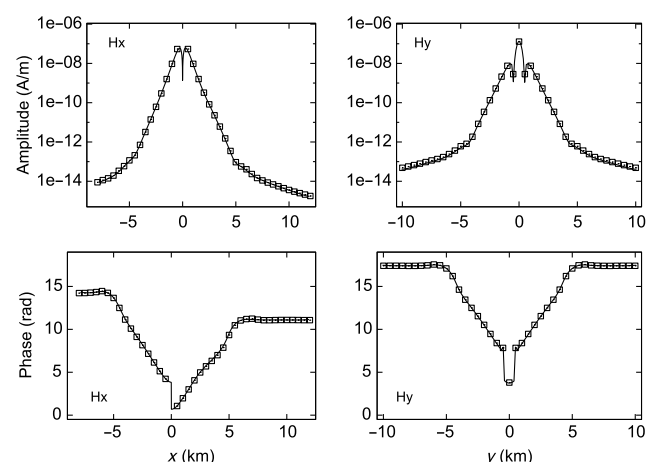


Figure 15. Comparison of the magnetic field responses for the model in Figure 13 calculated using the finite element method (line) and the integral equation method (open squares). The phase is unwrapped and the frequency is 1 Hz. The field values for the x -component and y -component are plotted along the receiver lines $y = 500$ m and $x = 500$ m, respectively.

for an electric dipole oriented in the x -direction and with a frequency of 0.1 Hz. The x -component values are plotted along the receiver line $y = 1000$ m, whereas the y -component values are plotted along the receiver line $y = 500$ m. The phase is plotted unwrapped for all components of the electric and magnetic fields. Figures 14, 15, 16, and 17 show a very good agreement between the integral equation and the edge finite element solutions for the electric field and the magnetic field, and within typical noise parameters in an experimental setup; for example, 2×10^{-15} V/m for the electric field (Um and Alumbaugh, 2007), and 10^{-6} nT²/Hz at 0.1 Hz for the magnetic field (using the specification of the magnetometer developed by the Scripps Institution of Oceanography).

MULTI-SOURCE SIMULATION

A peculiarity of using a multifrontal solver is the fact that the same matrix factorization can be used to achieve solutions for several right-hand sides. However, that requires that the simulation grid be refined near each source position, thus the grid dimensions can increase substantially, limiting the size of the model that can be considered. In this section, we present an example showing a grid setting for a multisource simulation, reusing the same matrix factorization.

Figure 18 illustrates the resistivity model and grid configuration utilized for this study. The resistivity model consists of a $3 \times 3 \times 0.3$ km³ parallelepiped body with resistivity 50 Ω m. The seawater resistivity is 0.3125 Ω m and is 1 km thick. The air was represented (not shown in Figure 18) with a 10 km and 10^4 Ω m resistive layer. The computational domain is discretized with a $161 \times 129 \times 49$ grid, representing a computational domain of $10 \times 9 \times 14$ km³, and corresponding to approximately 3.06 million degrees of freedom. In this example, we considered 63 source positions spaced 900 m in each direction, and the transmitter operating frequency is 0.25 Hz. For this simulation, we utilized 24 computer nodes with eight cores each. The primary field is computed using a resistivity model with two-half-spaces. The upper half-space

represents the air layer and the lower half-space has the resistivity of the seawater. The multisource solution requires the computation of the primary field for several source positions, thus increasing the computational load. To alleviate this problem, the calculation of the primary field for all sources is distributed over the computational nodes, meaning that 15 nodes compute the primary field responses for three sources and the remaining for two sources. Each node allocated an average of 3.6 GB of memory. The factorization wall-time is 786 s, and the back-substitution time for each source takes 21 s. Figures 19 and 20 compare the solutions for the x - and y -components of the electric field, for a source located at (0, -900, 45) m, using the grid setting in Figure 18 with the

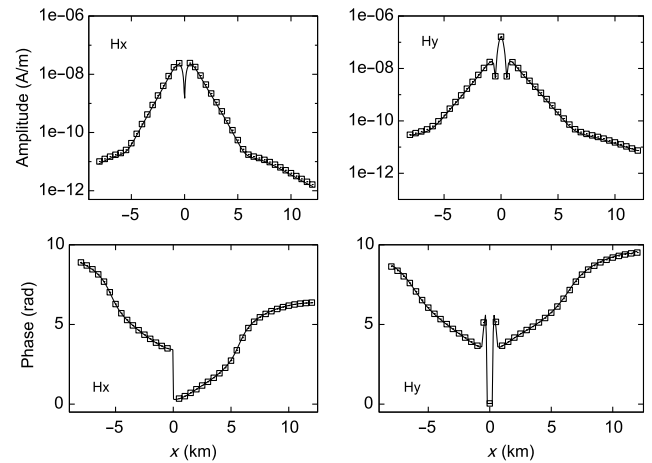


Figure 17. Comparison of the magnetic field responses for the model in Figure 13 calculated using the finite element method (line) and the integral equation method (open squares). The phase is unwrapped and the frequency is 0.1 Hz. The x -component is plotted along the receiver line $y = 1000$ m, and the y -component is plotted along the receiver line $y = 500$ m.

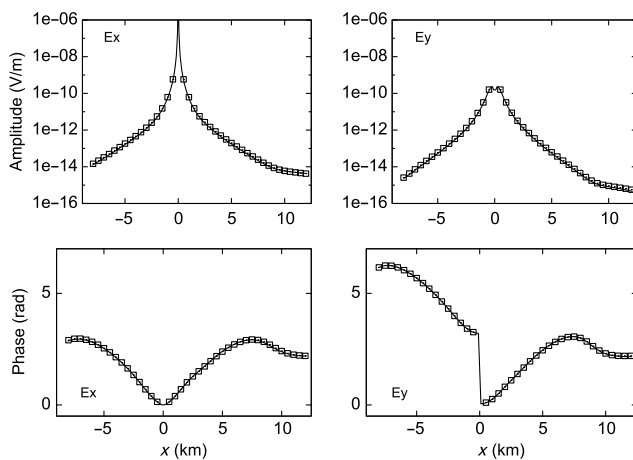


Figure 16. Comparison of the electric field responses for the model in Figure 13 calculated using the finite element method (line) and the integral equation method (open squares). The phase is unwrapped and the frequency is 0.1 Hz. The x -component is plotted along the receiver line $y = 0$ m, and the y -component is plotted along the receiver line $y = 500$ m.

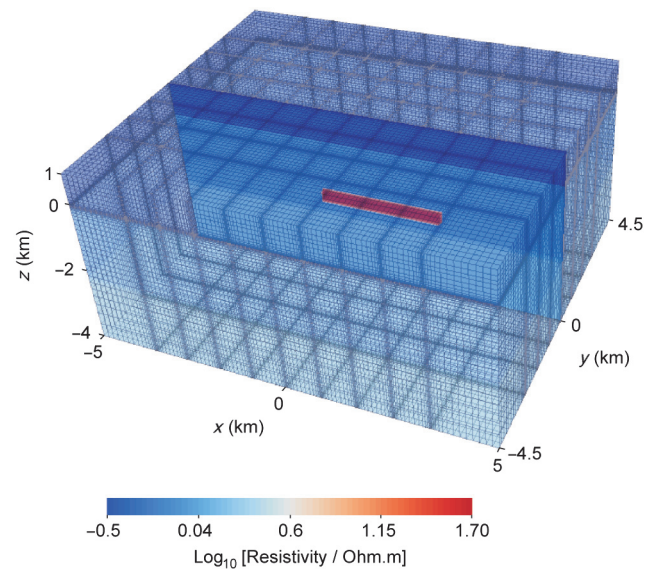


Figure 18. Resistivity model and grid utilized to test a multisource configuration.

solutions obtained utilizing a grid setting which is only finer near the source position (similar to the grid setting in Figure 9). The size of the grid refined around just one source is $91 \times 91 \times 49$, corresponding to approximately 1.21 million degrees of freedom. The task for the calculation of the field responses for one source only, was distributed over 24 nodes with eight cores each, taking 221 s to factorize and 7 s in the back-substitution. Each node allocated an average of 1.5 GB of RAM. The values in Figures 19 and 20 are plotted along receiver lines $y = -900$ m and $y = -1400$ m for the x - and y -components of the electric field, respectively. Figures 19 and 20, show errors below 5% for amplitude and below 0.03 rad for phase, showing that the grid setting utilized for the multisource solution is adequate and does not introduce major inaccuracies in the solution. The minimum and maximum grid spacing used on both

grid settings are 20 and 150 m, respectively. This example shows the use of a single factorization for achieving a multisource solution. It is necessary to use a single grid setting to allow the reutilization of the factors, and it is also required that for the refinement of the grid near each source position the computational needs increase substantially, imposing limitations to the size of the models that can be considered.

CONCLUSIONS

We presented a numerical scheme for 3D modeling of CSEM data by decomposing the electric field in primary and secondary components, and discretizing the equation for the secondary field utilizing edge finite elements. The edge finite element method is a discretization consistent with the discontinuity of the normal component of the electric field at interfaces across different materials, and enforces the divergence-free condition locally. In this work, we only considered Cartesian grids because this facilitates the task of building a grid and implement a grid generator in the code. The primary field is calculated using a homogeneous or two-half-space resistivity model; the latter is particularly important to improve the accuracy of the solution when the air is represented in the model. Comparisons between the solutions obtained using the edge finite element and 1D and 3D integral equation solutions demonstrated a very good agreement. The proposed approach is more computationally demanding in comparison to the integral equation solution; nonetheless, arbitrary resistivity models can be represented with significantly less effort. The method was also shown to be reliable in the range of frequencies typically used in CSEM surveys.

The linear system of equations obtained from the finite element method is solved using a multifrontal solver. The examples presented in this paper showed that the approach used for the numerical solution is robust, even for the indefinite system that results from the discretization of the Maxwell's equation for the electric field in the air, and for large grid spacing ratios. It was shown that it is possible to achieve a solution for relatively large models for one source in an acceptable run time. Nonetheless, it requires the use of large computational capabilities to cope with the computationally intensive multifrontal solver. Because the factorization is computationally very intensive, we reuse the factors to achieve a multiple source solution by successive forward and back-substitutions. However, this requires the grid to be refined at each source position, thus limiting the size of the models that can be considered and increasing the computational load, because the primary field has to be calculated for each source position. The latter is alleviated by distributing the calculation for multiple sources over the computing nodes.

The computation of the primary field is demanding, particularly when it is utilized a two-half-space and, by extension, a layered background model because the computation of Hankel transforms is necessary. This problem was mitigated by implementing a hybrid model of parallelism. The computation of the primary field is parallelized over the edges (for each source), using a shared memory model of parallelism, and over the number of sources using a distributed memory paradigm with message passing. A full field formulation has clear advantages in this aspect, as it is not necessary to compute the primary field, and therefore the computational overhead and complexity of the code can be significantly reduced.

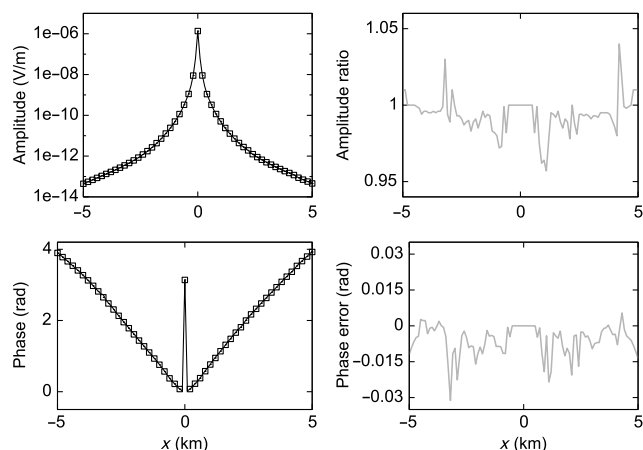


Figure 19. Comparison between the electric field responses for the x -component of the electric field, using the grid configuration shown in Figure 18, and a grid finer just at the source position $(0, -900, 45)$. The values are plotted along the receiver line $y = -900$ m and the phase is plotted unwrapped.

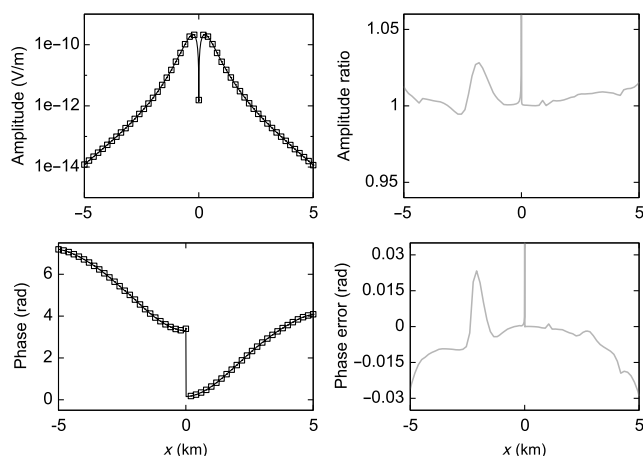


Figure 20. Comparison between the electric field responses for the y -component of the electric field, using the grid configuration shown in Figure 18, and a grid finer just at the source position $(0, -900, 45)$. The values are plotted along the receiver line $y = -1400$ m and the phase is plotted unwrapped.

Regarding the scalability of the solution of the linear system, there is a limit beyond which it is not possible to speed up the execution time by adding computing nodes. On the other hand, the average amount of allocated memory per node decreases with the increasing number of nodes, therefore making it possible to use systems with lower memory capabilities and/or preventing the system from running out of memory. As expected from the theoretical bounds, the number of floating point operations and workspace storage increases polynomially with the number of degrees of freedom, thus it is not possible to consider indefinitely bigger models with the current algorithmic approach and hardware.

The examples presented in this paper showed the usefulness of the approach for survey simulation and data inversion for limited sized models. They require, however, the use of a parallel computing system. Future plans include the extension of the method to consider anisotropy, and including effective representation of complex-shaped structures by decomposing the modeling domain with tetrahedra.

ACKNOWLEDGMENTS

The first author is sponsored by the Fundação para a Ciência e Tecnologia research grant SFRH/BD/40809/2007 under the POPH-QREN and the European Social Fund programs. The first author wishes to thank OHM Ltd. for making the 1D forward modeling code available and for providing the 3D synthetic data set. This work was developed using the Imperial College High Performance Computing facility and the authors are thankful to Simon Burbidge for all of his support. The authors wish to express their gratitude to Mark Everett, Stefan L. Helwig, and three anonymous reviewers for careful reading, suggestions, and constructive comments which helped to significantly improve the paper.

APPENDIX A

MULTIFRONTAL METHOD

This section provides a short review on the multifrontal method, using the notation of Liu (1992). Additional details can be found in Duff et al. (1986). Assuming that a matrix A has a Cholesky factorization $A = LL^T$ and is irreducible, that is each column of A and L has at least one off-diagonal nonzero, the elimination tree of A , is the set of nodes such that a node p is a parent node of j , if and only if

$$p = \min\{i > j : L_{ij} \neq 0\}. \quad (\text{A-1})$$

To illustrate the construction of the elimination tree, consider the fill-in pattern of L :

$$L = \begin{pmatrix} a & & & & & & \\ & b & & & & & \\ & & c & & & & \\ & \bullet & & d & & & \\ & & \bullet & \bullet & e & & \\ \bullet & \bullet & \bullet & & & \bullet & f \\ \bullet & & & & & \bullet & \bullet & g \end{pmatrix}. \quad (\text{A-2})$$

Figure A-1 shows the elimination tree for A-2 using condition A-1. The update matrix U_j is defined as

$$U_j = - \sum_{k \in T[j]-j} \begin{pmatrix} L_{j,k} \\ L_{i_1,k} \\ \vdots \\ L_{i_r,k} \end{pmatrix} \begin{pmatrix} L_{j,k} & L_{i_1,k} & \dots & L_{i_r,k} \end{pmatrix}, \quad (\text{A-3})$$

where i_0, i_1, \dots, i_r are the row subscripts of nonzeros in $L_{\bullet,k}$ and $i_0 = j$. Thus, the update matrix is formed by the outer-product contributions from the descendants of j . The multifrontal algorithm consists of repeating the following steps for all the columns:

- Set the locations of the nonzeros, j, i_1, \dots, i_r , in $L_{\bullet,k}$.
- Set the children nodes, c_1, \dots, c_s , of j in the elimination tree.
- Form the update matrix $U = U_{c_1} + \dots + U_{c_s}$.
- Set the j th frontal matrix:

$$F_j = \begin{pmatrix} a_{j,j} & a_{j,i_1} & \dots & a_{j,i_r} \\ a_{i_1,j} & & & \\ \vdots & & 0 & \\ a_{i_r,j} & & & \end{pmatrix} + U_j \quad (\text{A-4})$$

and factor F_j :

$$F_j = \begin{pmatrix} L_{j,j} & 0 \\ L_{i_1,j} & \\ \vdots & I \\ L_{i_r,j} & \end{pmatrix} \begin{pmatrix} 1 & 0 \\ & U_j \end{pmatrix} \begin{pmatrix} L_{j,j} & L_{i_1,j} & \dots & L_{i_r,j} \\ & & & I \end{pmatrix}. \quad (\text{A-5})$$

The parallel implementation of the multifrontal method essentially advances fronts while it creates and merges update matrices, U_j , and factorizes at least one column when the front advances. Once the factors are computed, the solution is obtained by forward and back-substitution.

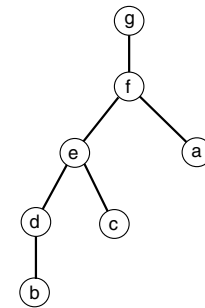


Figure A-1. Elimination tree for the matrix example in equation A-2.

REFERENCES

- Abubakar, A., T. M. Habashy, V. L. Druskin, L. Knizhnerman, and D. Alumbaugh, 2008, 2.5D forward and inverse modeling for interpreting low frequency electromagnetic measurements: *Geophysics*, **73**, no. 4, F165–F177, doi: [10.1190/1.2937466](https://doi.org/10.1190/1.2937466).
- Alumbaugh, D. L., G. A. Newman, L. Prevost, and J. Shadid, 1996, Three-dimensional wideband electromagnetic modelling on massively parallel computers: *Radio Science*, **31**, no. 1, 1–23, doi: [10.1029/95RS02815](https://doi.org/10.1029/95RS02815).
- Amestoy, P. R., I. S. Duff, J. Y. L'Excellent, and J. Koster, 2001, MUMPS: A general purpose distributed memory sparse solver: *Lecture Notes in Computer Science*, **1947**, 121–130, doi: [10.1007/3-540-70734-4](https://doi.org/10.1007/3-540-70734-4).
- Amestoy, P. R., I. S. Duff, and J.-Y. L'Excellent, 2000, Multifrontal parallel distributed symmetric and unsymmetric solvers: *Computer Methods in Applied Mechanics and Engineering*, **184**, 501–520, doi: [10.1016/S0045-7825\(99\)00242-X](https://doi.org/10.1016/S0045-7825(99)00242-X).
- Anderson, W., 1979, Numerical integration of related Hankel transforms of orders 0 and 1 by adaptive digital filtering: *Geophysics*, **44**, 1287–1305, doi: [10.1190/1.1441007](https://doi.org/10.1190/1.1441007).
- Andreis, D., and L. MacGregor, 2008, Controlled-source electromagnetic sounding in shallow water: Principles and applications: *Geophysics*, **73**, no. 1, F21–F32, doi: [10.1190/1.2815721](https://doi.org/10.1190/1.2815721).
- Aruliah, D. A., U. M. Ascher, E. Haber, and D. Oldenburg, 2001, A method for the forward modelling of 3D electromagnetic quasi-static problems: *Mathematical Models and Methods in Applied Sciences*, **11**, no. 1, 1–21, doi: [10.1142/S0218202501000702](https://doi.org/10.1142/S0218202501000702).
- Ashcraft, C., and J. W. H. Liu, 1998, Robust ordering of sparse matrices using multisection: *SIAM Journal on Matrix Analysis and Applications*, **19**, no. 3, 816–832, doi: [10.1137/S0895479896299081](https://doi.org/10.1137/S0895479896299081).
- Avdeev, D. B., A. V. Kuvshinov, O. V. Pankratov, and G. A. Newman, 2002, Three-dimensional induction logging problems, part I: An integral equation solution and model comparisons: *Geophysics*, **67**, 413–426, doi: [10.1190/1.1468601](https://doi.org/10.1190/1.1468601).
- Badea, E., M. Everett, G. Newman, and O. Biro, 2001, Finite-element analysis of controlled-source electromagnetic induction using Coulomb-gauged potentials: *Geophysics*, **66**, 786–799, doi: [10.1190/1.1444968](https://doi.org/10.1190/1.1444968).
- Behrens, J. P., 2005, The detection of electrical anisotropy in 35 ma Pacific lithosphere: Results from a marine controlled-source electromagnetic survey and implications for hydration of the upper mantle: Ph.D. thesis, University of California.
- Ben-Hadj-Ali, H., S. Operto, and J. Virieux, 2008, Velocity model building by 3D frequency-domain, full-waveform inversion of wide-aperture seismic data: *Geophysics*, **73**, no. 5, VE101–VE117, doi: [10.1190/1.2957948](https://doi.org/10.1190/1.2957948).
- Bondeson, A., T. Rylander, and P. Ingelstrom, 2005, *Computational electromagnetics*: Springer.
- Börner, R. U., O. Ernst, and K. Spitzer, 2008, Fast 3D simulation of transient electromagnetic fields by model reduction in the frequency domain using Krylov subspace projection: *Geophysical Journal International*, **173**, 766–780, doi: [10.1111/gji.2008.173.issue-3](https://doi.org/10.1111/gji.2008.173.issue-3).
- Bunch, J. R., and L. Kaufmann, 1977, Some stable methods for calculating inertia and solving symmetric linear systems: *Mathematics of Computation*, **31**, 163–163, doi: [10.1090/S0025-5718-1977-0428694-0](https://doi.org/10.1090/S0025-5718-1977-0428694-0).
- Chave, A., and C. Cox, 1982, Controlled electromagnetic sources for measuring electrical conductivity beneath the oceans. 1. Forward problem and model study: *Journal of Geophysical Research*, **87**, 5327–5338, doi: [10.1029/JB087iB07p05327](https://doi.org/10.1029/JB087iB07p05327).
- Chowdhury, I., and J. Y. L'Excellent, 2010, Some experiments and issues to exploit multicore parallelism in a distributed-memory parallel sparse direct solver: Technical report 7411, Institut National de Recherche en Informatique et en Automatique, Grenoble-Rhône-Alpes.
- Constable, S., 2005, Hydrocarbon exploration using marine EM techniques: OTC.
- Constable, S., and L. J. Smka, 2007, An introduction to marine controlled-source electromagnetic methods for hydrocarbon exploration: *Geophysics*, **72**, no. 2, WA3–WA12, doi: [10.1190/1.2432483](https://doi.org/10.1190/1.2432483).
- Datta, B. N., 2010, *Numerical linear algebra and applications*: SIAM.
- Druskin, V. L., L. A. Knizhnerman, and P. Lee, 1999, New spectral Lanczos decomposition method for induction modeling in arbitrary 3D geometry: *Geophysics*, **64**, 701–706, doi: [10.1190/1.1444579](https://doi.org/10.1190/1.1444579).
- Duff, I., A. Erisman, and J. Reid, 1986, *Direct methods for sparse matrices*: Oxford University Press.
- Eidesmo, T., S. Ellingsrud, L. M. MacGregor, S. Constable, M. C. Sinha, S. Johansen, F. N. Kong, and H. Westerdahl, 2002, Sea bed logging (SBL), a new method for remote and direct identification of hydrocarbons filled layers: *First Break*, **20**, 144–152.
- Ellingsrud, S., T. Eidesmo, S. Johansen, M. Sinha, L. MacGregor, and S. Constable, 2002, The meter reader-remote sensing of hydrocarbon layers by seabed logging (SBL): Results from a cruise offshore Angola: *The Leading Edge*, **21**, 972–982, doi: [10.1190/1.1518433](https://doi.org/10.1190/1.1518433).
- Germouche, A., J. Y. L'Excellent, and G. Utard, 2003, Impact of reordering on the memory of a multifrontal solver: *Parallel Computing*, **29**, 1191–1218, doi: [10.1016/S0167-8191\(03\)00099-1](https://doi.org/10.1016/S0167-8191(03)00099-1).
- Gould, N. I. M., Y. Hu, and J. A. Scott, 2005, A numerical evaluation of sparse direct solvers for the solution of large sparse, symmetric linear systems of equations: Technical Report RAL-TR-2005-005, Council for the Central Laboratory of the Research Councils.
- Haber, E., U. M. Ascher, D. A. Aruliah, and D. W. Oldenburg, 2000, Fast simulation of 3d electromagnetic problems using potentials: *Journal of Computational Physics*, **163**, 150–171, doi: [10.1006/jcph.2000.6545](https://doi.org/10.1006/jcph.2000.6545).
- Hursan, G., and M. Zhdanov, 2002, Contraction integral equation method in three-dimensional electromagnetic modeling: *Radio Science*, **37**, 1089, doi: [10.1029/2001RS002513](https://doi.org/10.1029/2001RS002513).
- Jackson, J., 1998, *Classical electrodynamics*, 3rd ed.: John Wiley & Sons.
- Jin, J., 2002, *Finite element method in electromagnetics*: Wiley-IEEE Press.
- Karypis, G., and V. Kumar, 1998, Multilevel algorithms for multi-constraint graph partitioning: Technical Report TR 98-019: Department of Computer Science, University of Minnesota.
- Liseikin, V., 2009, *Grid generation methods*: Springer.
- Liu, J. W. H., 1992, The multifrontal method for sparse matrix solution: Theory and practice: *SIAM Review*, **34**, 141–153, doi: [10.1137/1034028](https://doi.org/10.1137/1034028).
- MacGregor, L., M. Sinha, and S. Constable, 2001, Electrical resistivity structure of the Valu Fa ridge, Lau basin, from marine controlled-source electromagnetic sounding: *Geophysical Journal International*, **146**, 217–236, doi: [10.1046/j.1365-246X.2001.00440.x](https://doi.org/10.1046/j.1365-246X.2001.00440.x).
- Monk, P., 2003, *Finite element methods for Maxwell's equations*: Oxford University Press.
- Nedelec, J. C., 1980, Mixed finite elements in R3: *International Journal for Numerical and Analytical Methods in Geomechanics*, **35**, 315–341.
- Newman, G., and D. Alumbaugh, 1995, Frequency-domain modelling of airborne electromagnetic responses using staggered finite differences: *Geophysical Prospecting*, **43**, no. 8, 1021–1042, doi: [10.1111/gpr.1995.43.issue-8](https://doi.org/10.1111/gpr.1995.43.issue-8).
- Newman, G., and D. Alumbaugh, 2002, Three-dimensional induction logging problems, Part 2: A finite-difference solution: *Geophysics*, **67**, 484–491, doi: [10.1190/1.1468608](https://doi.org/10.1190/1.1468608).
- Oldenburg, D. W., E. Haber, and R. Shekhtman, 2008, Forward modelling and inversion of multi-source TEM data: 78th Annual International Meeting, SEG, Expanded Abstracts, 559.
- Operto, S., J. Virieux, P. Amestoy, J.-Y. L'Excellent, L. Giraud, and H. B. H. Ali, 2007, 3D finite-difference frequency-domain modeling of visco-acoustic wave propagation using a massively parallel direct solver: A feasibility study: *Geophysics*, **72**, no. 5, SM195–SM211, doi: [10.1190/1.2759835](https://doi.org/10.1190/1.2759835).
- Orange, A., K. Key, and S. Constable, 2009, The feasibility of reservoir monitoring using time-lapse marine CSEM: *Geophysics*, **74**, no. 2, F21–F29, doi: [10.1190/1.3059600](https://doi.org/10.1190/1.3059600).
- Plessix, R., M. Darnet, and W. Mulder, 2007, An approach for 3D multi-source, multifrequency CSEM modeling: *Geophysics*, **72**, no. 5, SM177–SM184, doi: [10.1190/1.2744234](https://doi.org/10.1190/1.2744234).
- Rodrigue, G., and D. White, 2001, A vector finite element time-domain method for solving Maxwell's equations on unstructured hexahedral grids: *SIAM Journal on Scientific Computing*, **23**, no. 3, 683–706, doi: [10.1137/S1064827598343826](https://doi.org/10.1137/S1064827598343826).
- Saad, Y., 2003, *Iterative methods for sparse linear systems*, second edition: SIAM.
- Spichak, V. V., 2006, A method for constructing high-order differential boundary conditions for solving external boundary value problems in geoelectromagnetism: *Izvestiya Russian Academy of Sciences, Physics of the Solid Earth*, **42**, no. 3, 193–200, doi: [10.1134/S1069351306030025](https://doi.org/10.1134/S1069351306030025).
- Smka, L. J., J. J. Carazzone, M. S. Ephron, and E. A. Eriksen, 2006, Remote reservoir resistivity mapping: *The Leading Edge*, **25**, 972–975, doi: [10.1190/1.2335169](https://doi.org/10.1190/1.2335169).
- Streich, R., 2009, 3D finite-difference frequency-domain modeling of controlled-source electromagnetic data: Direct solution and optimization for high accuracy: *Geophysics*, **74**, no. 5, F95–F105, doi: [10.1190/1.3196241](https://doi.org/10.1190/1.3196241).
- Streich, R., and M. Becken, 2011, Electromagnetic fields generated by finite-length wire sources: Comparison with point dipole solutions: *Geophysical Prospecting*, **59**, 361–374, doi: [10.1111/gpr.2011.59.issue-2](https://doi.org/10.1111/gpr.2011.59.issue-2).
- Torquill Smith, J., 1996, Conservative modeling of 3D electromagnetic fields, part II: Bi-conjugate gradient solution and an accelerator: *Geophysics*, **61**, 1319–1324, doi: [10.1190/1.1444055](https://doi.org/10.1190/1.1444055).
- Tyler, R. H., F. Vivier, and S. Li, 2004, Three-dimensional modelling of the ocean electrodynamics using gauged potentials: *Geophysical Journal International*, **158**, 874–887, doi: [10.1111/j.1365-246X.2004.02318.x](https://doi.org/10.1111/j.1365-246X.2004.02318.x).

- Um, E. S., and D. L. Alumbaugh, 2007, On the physics of the marine controlled-source electromagnetic method: *Geophysics*, **72**, no. 2, WA13–WA26, doi: [10.1190/1.2432482](https://doi.org/10.1190/1.2432482).
- Um, E. S., D. L. Alumbaugh, and J. M. Harris, 2010, A Lorenz-gauged finite-element solution for transient CSEM modeling: 80th Annual International Meeting, SEG, Expanded Abstracts, 748–752.
- van der Vorst, H., 2003, Iterative Krylov methods for large scale linear systems: Cambridge University Press.
- Ward, S. H., and G. W. Hohmann, 1988, Electromagnetic theory for geophysical applications, in M. N. Nabighian, ed. *Electromagnetic methods in applied geophysics — Theory*, vol. **1**, SEG, 131–311.
- Yee, K., 1966, Numerical solution of initial boundary value problems involving Maxwell's equations in isotropic media: *IEEE Transactions on Antennas and Propagation*, **14**, 302–307, doi: [10.1109/TAP.1966.1138693](https://doi.org/10.1109/TAP.1966.1138693).
- Yilmaz, O., 2001, *Seismic data analysis*: SEG.
- Zhdanov, M. S., S. K. Lee, and K. Yoshioka, 2006, Integral equation method for 3D modeling of electromagnetic fields in complex structures with inhomogeneous background conductivity: *Geophysics*, **71**, no. 6, G333–G345, doi: [10.1190/1.2358403](https://doi.org/10.1190/1.2358403).
- Zienkiewicz, O. C., and R. L. Taylor, 2005, *The finite element method set*, 6th ed.: Butterworth-Heinemann.